Non-linear vibrations of imperfect free-edge circular plates and shells

Cédric Camier, Cyril Touzé, Olivier Thomas

Non-linear vibrations of imperfect free-edge circular plates and shells

C. Camier [a], C. Touzé [a,*], O. Thomas [b]

[a] ENSTA-UME, Unité de Mécanique, Chemin de la Hunière, 91761 Palaiseau Cedex, France
[b] CNAM, LMSSC, Laboratoire de Mécanique des structures et systèmes couplés, 2, rue Conté, 75003 Paris, France

A B S T R A C T

Large-amplitude, geometrically non-linear vibrations of free-edge circular plates with geometric imper-fections are addressed in this work. The dynamic analog of the von Kármán equations for thin plates, with a stress-free initial deflection, is used to derive the imperfect plate equations of motion. An expansion onto the eigenmode basis of the perfect plate allows discretization of the equations of motion. The associated non-linear coupling coefficients for the imperfect plate with an arbitrary shape are analytically expressed as functions of the cubic coefficients of a perfect plate. The convergence of the numerical solutions are systematically addressed by comparisons with other models obtained for specific imperfections, showing that the method is accurate to handle shallow shells, which can be viewed as imperfect plate. Finally, comparisons with a real shell are shown, showing good agreement on eigenfrequencies and mode shapes. Frequency-response curves in the non-linear range are compared in a very peculiar regime displayed by the shell with a 1:1:2 internal resonance. An important improvement is obtained compared to a perfect spherical shell model, however some discrepancies subsist and are discussed.

1. Introduction

Geometric imperfections have been recognized since a long time for having a major effect on the linear and non-linear characteristics of thin-walled structures: from one structure to another one, even though manufactured by the same technique, it has been observed that eigenfrequencies and buckling loads can be different. In particular, a number of experimental and theoretical studies conducted in the 60–80s of the last century clearly establish that the initial deflection of thin structures such as plates and shells, that are unfortunately unavoidable when dealing with real structures, is a major cause for explaining the important discrepancies observed between theoretical results (calculated with an assumed perfect structure) and experimental observations (Donnell, 1976; Chia, 1980; Coppa, 1966; Tobias, 1951; Kubenko and Koval'chuk, 2004). Other important factors that could have been incriminated such as inaccuracy in the boundary conditions, inhomogeneity of the material or slight variations of the thickness, are not considered in this study and have been addressed in Chen et al. (2005), Gupta et al. (2007).

Among other thin shells, circular cylindrical shell with imperfections have been thoroughly studied, because of their wide importance in various engineering fields. The first investigations on the subject were generally limited to the effect of axisymmetric imperfections on the buckling loads (Koiter, 1963; Rosen and Singer, 1974). Asymmetric imperfections were then introduced in Rosen and Singer (1976). Geometrically non-linear, large-amplitude vibrations are considered in Gonçalves (1994). Recent papers give overview of the numerous results available for cylindrical shells, where forced and parametric excitation, flutter, experimental measurements of imperfections and fitting to theoretical models, are detailed, see Amabili (2003), Amabili and Païdoussis (2003), Kubenko and Koval'chuk (2004) and references therein.

The influence of imperfections on the behaviour of plates has also been reported by many investigations. Rectangular plates are generally treated for their wide use in practice, as well as for the ease of using Cartesian co-ordinates. Free vibrations with large amplitude are treated in Celep (1976). Quantitative results on the effect of an imperfection on eigenfrequencies and buckling loads are given in Hui and Leissa (1983). The type of non-linearity (hardening or softening behaviour of non-linear oscillations) is also addressed by Hui (1984). These two studies clearly establish that large deviations from the perfect theory are present, for amplitude of imperfections being only a fraction of the plate thickness. However, all the presented results are obtained via a crude approximation consisting in keeping only one mode in the Galerkin expansion, so that some of their results must be reconsidered with more accurate expansions. Forced vibrations with experimental results are shown in Yamaki and Chiba (1983), Yamaki et al. (1983). The transition from the hardening behaviour of flat plates

* Corresponding author.
E-mail addresses: cedric.camier@ensta.fr (C. Camier), cyril.touze@ensta.fr

to the softening behaviour of imperfect rectangular plates is also addressed in Lin and Chen (1989), as well as in Ostiguy and Sassi (1992), where the response to simultaneous forced and parametric excitation is investigated.

The case of circular plates has received less attention. Hui, with a single-mode expansion and axisymmetric restriction, studied the type of non-linearity with various (mainly clamped and simply supported) boundary conditions (Hui, 1983). Yamaki et al., with a three-mode expansion and also with an axisymmetric restriction, studied both theoretically and experimentally the forced response of clamped circular plates (Yamaki et al., 1981a, 1981b).

In all the precedent studies, the method used for analyzing the results is in most of the cases a Galerkin expansion, based either on ad-hoc basis functions, or on the eigenmodes of the perfect structure. However, a number of them used a single-mode expansion, see e.g. Celep (1976), Hui and Leissa (1983), Hui (1984), Lin and Chen (1989), Hui (1983). As precised by a number of studies (Yamaki and Chiba, 1983; Yamaki et al., 1981a; Ilanko, 2002), these truncations are too severe and may lead to incorrect results, especially when dealing with non-linear vibrations. More particularly, it has been demonstrated in Nayfeh et al. (1992), Touzé et al. (2004) that, when predicting the type of non-linearity (hardening/softening behaviour) of a structure with an initial curvature, single-mode truncation leads to erroneous results.

The aim of the present study is thus to reconsider some of the precedent results on imperfect plates, while specifically overstepping the limitations underlined in the current state-of-the-art. More particularly, the following points are addressed. Firstly, the axisymmetric restriction for the case of circular plates is not retained. Secondly, free-edge boundary conditions, that are generally not treated in the literature, are considered. Thirdly, a Galerkin expansion using an arbitrary number of expansion functions is used, hence overstepping the usual limitation to a one-mode expansion. The initial shape of the structure as well as its deflection in vibrations are expanded on the same expansion functions, the mode shapes of a circular plate. It leads to analytical expressions of the coupling coefficients, as functions of the non-linear cubic coefficients of the perfect plate. The convergence of the numerical solutions is systematically addressed by comparing the obtained results with the spherical shallow shell model developed in Thomas et al. (2005b), as well as with finite-elements solutions. It is shown that converged solutions are available with a reasonable number of expansion functions, for amplitudes of imperfections up to 30 times the thickness of the plate. This allows considering a shallow shell model directly from a plate model.

Finally, comparisons with experimental results on a real shell are reported. Numerical problems related to the approximation of the measured geometry are discussed. The linear results provided by the imperfect plate model are compared to measurements, showing an important improvement with comparison to the predictions brought by a perfect shallow shell model. At the non-linear level, frequency-response curves are drawn, in the specific regime obtained when forcing the first axisymmetric mode, the eigenfrequency of which is twice those of the two companion modes with six nodal diameters. The complete experimental report has already been addressed in Thomas et al. (2007), showing that the non-linear terms predicted by a perfect spherical shell model are very far from the measured ones. Although showing a better agreement with experiment, some discrepancies subsist in some non-linear coefficients, giving an incorrect prediction of the instability regions. Finally the complete model predicts the correct type of non-linearity of the shell, but with an enhanced non-linearity.

2. Theoretical formulation

2.1. General case

2.1.1. Local equation

A thin plate of diameter $2a$ and thickness h (with $h \ll a$), made of a homogeneous isotropic material of density ρ, Poisson's ratio ν and Young's modulus E, is considered. The equations of motion for perfect circular plates subjected to large deflections, moderate rotations and with small strain, used in the sequel, are known as the dynamic analogues of the von Kármán equations, where damping and forcing have been added. In-plane and rotatory inertia are neglected so that an Airy stress function F is used. Hence, at a given point of co-ordinates (r,θ), the equations of motion are given in terms of the Airy stress function F and the transverse displacement w along the normal to the mid-surface of the plate, for all time t:

$$D\Delta\Delta w + \rho h\ddot{w} = L(w,F) - c\dot{w} + p, \tag{1a}$$

$$\Delta\Delta F = -\frac{Eh}{2}L(w,w), \tag{1b}$$

where

$$L(w,F) = w_{,rr}\left(\frac{F_{,r}}{r} + \frac{F_{,\theta\theta}}{r^2}\right) + F_{,rr}\left(\frac{w_{,r}}{r} + \frac{w_{,\theta\theta}}{r^2}\right) - 2\left(\frac{w_{,r\theta}}{r} - \frac{w_{,\theta}}{r^2}\right)\left(\frac{F_{,r\theta}}{r} - \frac{F_{,\theta}}{r^2}\right), \tag{2}$$

$D = Eh^3/12(1-\nu^2)$ is the flexural rigidity, c is a viscous damping coefficient and p represents the external load normal to the surface of the plate. $(\ddot{\ })$ denotes a twice differentiation with respect to time t and $(\cdot)_{,\alpha\beta}$ is the partial derivative with respect to α and β. The expression of the Airy stress function F as a function of the membrane stresses can be found in Touzé et al. (2002). Laplacian operator writes:

$$\Delta(\cdot) = (\cdot)_{,rr} + \frac{1}{r}(\cdot)_{,r} + \frac{1}{r^2}(\cdot)_{,\theta\theta}. \tag{3}$$

As shown in Fig. 1, the geometric imperfections are included in the formulation by splitting the transverse displacement w into a static part w_0 and a dynamic part $\tilde{w}$, so that:

$$w(r,\theta,t) = \tilde{w}(r,\theta,t) + w_0(r,\theta). \tag{4}$$

In order to satisfy the static equilibrium initial state, both p and F are similarly split in two quantities, a time-dependent one and a static one:

$$F = \tilde{F} + F_0, \tag{5a}$$

$$p = \tilde{p} + p_0. \tag{5b}$$

Substituting Eqs. (5) in Eqs. (1), one obtains:

$$D\Delta\Delta\tilde{w} + D\Delta\Delta w_0 + \rho h\ddot{\tilde{w}} = L(\tilde{w},\tilde{F}) + L(w_0,\tilde{F}) + L(\tilde{w},F_0) + L(w_0,F_0) - c\dot{\tilde{w}} + \tilde{p} + p_0, \tag{6a}$$

$$\Delta\Delta\tilde{F} + \Delta\Delta F_0 = -\frac{Eh}{2}\left[L(\tilde{w},\tilde{w}) + 2L(\tilde{w},w_0) + L(w_0,w_0)\right]. \tag{6b}$$

The static equilibrium leads to the following relationships:

$$D\Delta\Delta w_0 = L(w_0,F_0) + p_0, \tag{7a}$$

$$\Delta\Delta F_0 = -\frac{Eh}{2}L(w_0,w_0). \tag{7b}$$

Since a purely geometric imperfection, without initial in-plane stress, is considered in this study, the static membrane stress term

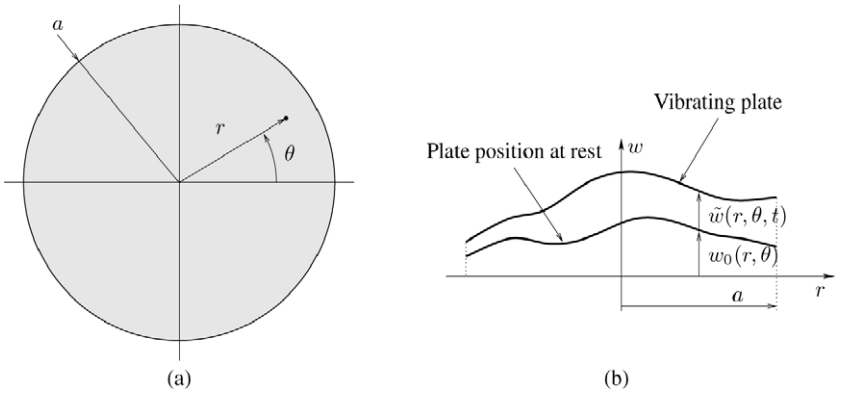

Fig. 1. Definition of the geometric imperfection w_0. (a) Top view with polar coordinates. (b) Cross-section on a selected radius.

F_0 is enforced to zero, so that the non-linear partial differential equations (PDEs) governing the motion of the imperfect circular plate reads:

$$D\Delta\Delta\tilde{w} + \rho h\ddot{\tilde{w}} = L(\tilde{w},\tilde{F}) + L(w_0,\tilde{F}) - c\dot{\tilde{w}} + \tilde{p}, \tag{8a}$$

$$\Delta\Delta\tilde{F} = -\frac{Eh}{2}\big[L(\tilde{w},\tilde{w}) + 2L(\tilde{w},w_0)\big]. \tag{8b}$$

As longitudinal inertia is neglected, $\tilde{F}$ is slaved to transverse displacement via Eq. (8b). Because of the bilinearity property of $L(\cdot,\cdot)$, Eq. (8b) shows that F contains both a linear and a quadratic term in $\tilde{w}$, the linear one being directly related to the imperfections w_0. In the right-hand side of Eq. (8b), $L(w_0,\tilde{F})$ is then responsible for a linear coupling between transverse motion and membrane stretching, stemming from the geometric imperfections. This term, together with $L(\tilde{w},\tilde{F})$, also produces a quadratic non-linear term, explained by the loss of symmetry of the imperfect plate in the transverse direction. Finally, in the same manner than for a perfect plate, a cubic non-linear term is created by $L(\tilde{w},\tilde{F})$, which is independent of w_0.

2.1.2. Free-edge boundary conditions

Boundary conditions are similar to those of a free-edge perfect circular plate (Touzé et al., 2002), as well as those of a shallow spherical shell (Thomas et al., 2005b). Their expressions stem for the vanishing of the external loads at the edge. They read, for all t and θ:

$$\tilde{F} \text{ and } \tilde{w} \text{ are bounded at } r=0, \tag{9a}$$

$$\tilde{F}_{,r} + \frac{1}{a}\tilde{F}_{,\theta\theta} = 0, \quad \tilde{F}_{,r\theta} + \frac{1}{a}\tilde{F}_{,\theta} = 0, \quad \text{at } r=a, \tag{9b}$$

$$\tilde{w}_{,rr} + \frac{\nu}{a}\tilde{w}_{,r} + \frac{\nu}{a^2}\tilde{w}_{,\theta\theta} = 0, \quad \text{at } r=a, \tag{9c}$$

$$\tilde{w}_{,rrr} + \frac{1}{a}\tilde{w}_{,rr} - \frac{1}{a^2}\tilde{w}_{,r} + \frac{2-\nu}{a^2}\tilde{w}_{,r\theta\theta} - \frac{3-\nu}{a^3}\tilde{w}_{,\theta\theta} = 0, \quad \text{at } r=a. \tag{9d}$$

2.1.3. Dimensionless equations

In order to balance the magnitude of all involved quantities, the equations are rewritten in dimensionless form, by introducing:

$$\tilde{w} = h\bar{\tilde{w}}, \quad w_0 = h\bar{w}_0, \quad r = a\bar{r}. \tag{10}$$

Dimensionless factors are defined as followed:

$$\tilde{F} = Eh^3\bar{\tilde{F}}, \qquad t = \sqrt{\frac{\rho h a^4}{D}}\bar{t},$$
$$p = \frac{h^4E}{a^4}\bar{p}, \qquad c = \frac{Eh^3}{2a^2}\sqrt{\frac{\rho h}{D}}\bar{c} \tag{11}$$

Substituting the above definitions in Eqs. (8) and dropping the overbars in the results for the sake of clearness, equations of motion of imperfect plates with free-edge and subjected to large deflection finally writes:

$$\Delta\Delta\tilde{w} + \ddot{\tilde{w}} = \varepsilon\big[L(\tilde{w},\tilde{F}) + L(w_0,\tilde{F}) - 2\mu\dot{\tilde{w}} + \tilde{p}\big], \tag{12a}$$

$$\Delta\Delta\tilde{F} = -\frac{1}{2}\big[L(\tilde{w},\tilde{w}) + 2L(\tilde{w},w_0)\big], \tag{12b}$$

with $\varepsilon = 12(1-\nu^2)$.

2.1.4. Modal expansion

In this section, the equations of motion (12) are discretized by expanding the unknowns w, w_0 and F onto the eigenmodes of the linear system associated to Eqs. (1a), (1b) via:

$$w_0(r,\theta) = \sum_{p=1}^{N_0} a_p\Phi_p(r,\theta) + z_g, \tag{13a}$$

$$\tilde{w}(t,r,\theta) = \sum_{p=1}^{N_w} q_p(t)\Phi_p(r,\theta), \tag{13b}$$

$$\tilde{F}(t,r,\theta) = \sum_{p=1}^{N_F} \eta_p(t)\Psi_p(r,\theta). \tag{13c}$$

In the above equations, the $\{\Phi_i\}_{i\in\mathbb{N}}$ are the transverse vibration mode shapes of the perfect plate and the $\{\Psi_i\}_{i\in\mathbb{N}}$ are membrane modes, defined by, for all $i\in\mathbb{N}^*$:

$$\Delta\Delta\Phi_i - \omega_i^2\Phi_i = 0, \tag{14a}$$

$$\Delta\Delta\Psi_i - \zeta_i^4\Psi_i = 0, \tag{14b}$$

together with boundary conditions (9a)–(9c) for Φ_i and (9b), (9c) for Ψ_i. In the above equations, ω_i is the i-th natural flexural frequency of the perfect plate. The analytical expressions for Φ_i and Ψ_i as well numerical values for ω_i and ζ_i can be found in Touzé et al. (2002). Moreover, shape functions $\{\Phi_i\}_{i\in\mathbb{N}}$ and $\{\Psi_i\}_{i\in\mathbb{N}}$ are assumed to be normalized, so that for all $p\in[1\ N_w]$,

$$\iint_S \Phi_p^2\,dS = 1, \qquad \iint_S \Psi_p^2\,dS = 1 \tag{15}$$

where S is the surface of the plate, i.e. the domain defined by $(r,\theta)\in[0\ 1]\times[0\ 2\pi]$. By using the orthogonality property of the eigenmodes, amplitudes a_p and center of mass' offset z_g write:

$$a_p = \iint_S w_0\Phi_p\,dS, \tag{16a}$$

$$z_g = \iint_S w_0\,dS. \tag{16b}$$

In Eqs. (13a)–(13c), N_0 and N_w are the number of transverse eigenfunctions and N_F the number of in-plane eigenfunctions, selected for discretizing the system. In the numerical results presented in the sequel, N_F has been fixed to 12, a sufficient value for obtaining a 5-digits accuracy for the cubic non-linear coefficients, as already shown in Touzé et al. (2002), Thomas et al. (2005b). On the other hand, N_0 and N_w remain variable so as to study the convergence of the results. By multiplying Eq. (12b) by Ψ_u, Eq. (12a) by Φ_u, integrating both results over the surface S of the plate, and using the orthogonality property of the modes, one obtains the following set of oscillators with linear and non-linear coupling terms, for all $u \in [1\ N_w]$:

$$\ddot{q}_u + \omega_u^2 q_u = -\varepsilon \left[\sum_{p=1}^{N_w} \alpha_p^u q_p + \sum_{p=1}^{N_w}\sum_{r=1}^{N_w} \beta_{pr}^u q_p q_r + \sum_{p=1}^{N_w}\sum_{r=1}^{N_w}\sum_{s=1}^{N_w} \Gamma_{rsp}^u q_p q_r q_s + 2\mu\dot{q}_u - \tilde{p}_u \right]. \tag{17}$$

Expressions for $\tilde{p}_u$ and Γ_{rsp}^u are, according to Eqs. (15):

$$\tilde{p}_u = \iint_S \Phi_u(r,\theta)\tilde{p}(r,\theta,t)\,dS, \tag{18a}$$

$$\Gamma_{rsp}^u = -\frac{1}{2}\sum_{q=1}^{N_F} \frac{1}{\xi_q^4} \iint_S \Phi_u L(\Phi_p, \Psi_q) \iint_S \Psi_q L(\Phi_r, \Phi_s)\,dS. \tag{18b}$$

The cubic coefficients Γ_{rsp}^u are those of the perfect case, presented in Touzé et al. (2002). The new linear and quadratic coupling coefficients α_p^u and β_{pr}^u appearing in Eq. (17) stem from the geometric imperfection w_0, and are thus expressed as functions of the amplitudes a_p of the expansion of w_0 introduced in Eq. (13a). They write:

$$\alpha_p^u = -\sum_{r=1}^{N_0}\sum_{s=1}^{N_0} 2\Gamma_{rps}^u a_r a_s, \tag{19a}$$

$$\beta_{pr}^u = -\sum_{s=1}^{N_0} (\Gamma_{rps}^u + 2\Gamma_{srp}^u) a_s, \tag{19b}$$

Thanks to the projection of the imperfection onto the perfect plate's natural modes, one obtains very simple expressions for the coefficients α_p^u and β_{pr}^u for a plate with an arbitrary imperfection. Indeed, these specific coefficients can be computed easily, once the cubic non-linear coefficients of the perfect circular plate are known. This property is the main advantage of the present formulation, as any imperfection is expressed from the perfect case through very simple analytical formulas. In order to compare the linear characteristics (eigenfrequencies, mode shapes) and non-linear coefficients of the imperfect plate with benchmark cases, one can also write Eq. (17) in the basis of the eigenvectors of the imperfect structure. Let $\mathbf{A} = \{\varepsilon\alpha_p^u + \omega_u^2\delta_{up}\}_{u,p\in[1;N_w]}$ be the linear part of (17) in matrix form. Diagonalization of $\mathbf{A}$ gives numerically the eigenfrequencies and mode shapes of the imperfect plate by the formula:

$$\{\Omega_u \delta_{up}\}_{u,p\in[1;N_w]} = \mathbf{P}^{-1}\mathbf{A}\mathbf{P}, \tag{20}$$

where $\mathbf{P}$ is the matrix of eigenvectors. Applying the change of coordinates $\mathbf{q} = \mathbf{P}\mathbf{X}$ with $\mathbf{q} = \{q_i\}_{i\in[1;N_w]}$ and $\mathbf{X} = \{X_i\}_{i\in[1;N_w]}$, one can write:

$$\ddot{X}_u + \Omega_u^2 X_u = -\varepsilon \left[\sum_{p=1}^{N_w}\sum_{r=1}^{N_w} g_{pr}^u X_p X_r + \sum_{p=1}^{N_w}\sum_{r=1}^{N_w}\sum_{s=1}^{N_w} h_{rsp}^u X_p X_r X_s - 2\mu_u \dot{X}_u + \tilde{G}_u \right], \tag{21}$$

where the X_u are the modal coordinates, associated to the imperfect plate eigenmodes. A modal damping term μ_u is assumed, G_u is the modal forcing, and g_{pr}^u and h_{rsp}^u are the new coupling coefficients of the imperfect plate. Denoting by P_{ij} the generic term of matrix $\mathbf{P}$, and P_{ij}^{-1} the one of $\mathbf{P}^{-1}$, they read:

$$g_{pr}^u = \sum_{i,j,k=1}^{N_w} \beta_{jk}^i P_{ui}^{-1} P_{jp} P_{kr}, \tag{22a}$$

$$h_{rsp}^u = \sum_{i,j,k,n=1}^{N_w} \Gamma_{jkn}^i P_{ui}^{-1} P_{jr} P_{ks} P_{np}. \tag{22b}$$

2.2. Validation: the case of a spherical imperfection

2.2.1. Asymptotic expansion and comparison

When a spherical imperfection is considered, the circular plate becomes a shallow spherical shell. The corresponding equations of motion have been thoroughly analyzed in Thomas et al. (2005b) and the linear (eigenfrequencies and mode shapes) as well as non-linear characteristics have been directly obtained, providing a reference solution. Consequently, the results of the present model can be compared to those from Thomas et al. (2005b). Firstly, the PDEs of motion are compared. A spherical imperfection w_0 with height H, and curvature R, writes, in its dimensionless form:

$$w_0(r) = \frac{1}{h}\left(\sqrt{R^2 - a^2 r^2} + H - R\right), \tag{23}$$

with

$$H = R - \sqrt{R^2 - a^2}. \tag{24}$$

With the shallow assumption $a/R \ll 1$, a first-order Taylor expansion of the spherical imperfection expression defined by Eq. (23), as well as $L(w_0, \tilde{F})$ and $L(\tilde{w}, w_0)$ appearing in Eqs. (12), yields respectively:

$$w_0(r) = \frac{1}{h}\left(H - \frac{a^2 r^2}{2R}\right) + \mathcal{O}\left(\frac{a}{R}\right), \tag{25a}$$

$$L(w_0, \tilde{F}) = -\frac{a^2}{Rh}\Delta\tilde{F} + \mathcal{O}\left(\frac{a}{R}\right), \tag{25b}$$

$$L(\tilde{w}, w_0) = -\frac{a^2}{Rh}\Delta\tilde{w} + \mathcal{O}\left(\frac{a}{R}\right). \tag{25c}$$

Substituting these approximate terms into Eqs. (12), the PDEs of motion of the shallow spherical shell are those obtained in Thomas et al. (2005b):

$$\Delta\Delta w + \frac{Rh}{a^2}\chi\Delta F + \ddot{w} = \varepsilon L(w, F) + \varepsilon\frac{a^2}{Rh}[-2\mu\dot{w} + p], \tag{26a}$$

$$\Delta\Delta F - \frac{a^2}{Rh}\Delta w = -\frac{1}{2}L(w, w), \tag{26b}$$

where

$$\chi = 12\left(1 - \nu^2\right)\frac{a^4}{R^2 h^2} \tag{27}$$

is the only free geometrical parameter. This analytic development shows that the equations of the shallow shell are recovered when only the first-order term of the geometric imperfection is considered. Hence the shallow spherical shell model described by Eqs. (26) is closer to a parabolic shell model, as the leading term of the asymptotic expansion (25a) is quadratic in the radius r, whereas the present model with an exact expansion of the spherical imperfection should be valid for a larger range of imperfection amplitudes. This will be further discussed in the next sections where numerical comparisons are given.

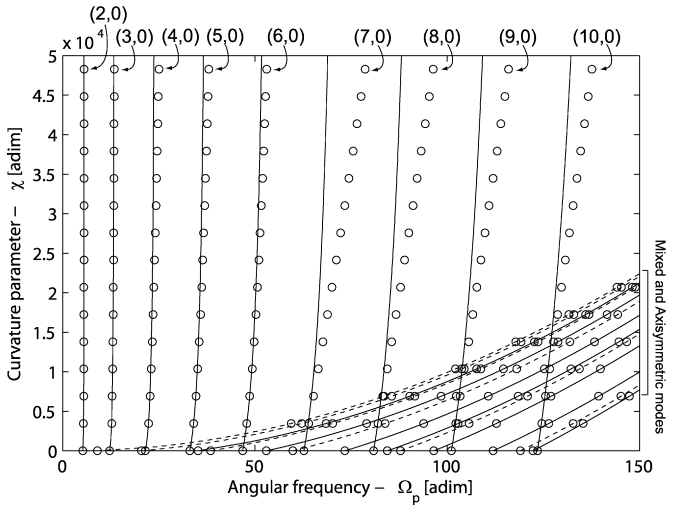

Fig. 2. Dimensionless natural angular frequencies Ω_p of a spherical shell with respect to curvature parameter χ, according to the spherical shell model (Thomas et al., 2005b) (−) and calculated with the imperfect plate model in which a spherical imperfection is selected (o). Mixed and axisymmetric modes indicated to the right are, by order of appearance: $(0,1)$, $(1,1)$, $(2,1)$, $(0,2)$, $(3,1)$, $(1,2)$, $(4,1)$, $(2,2)$, $(0,3)$, $(5,1)$, $(3,2)$, $(1,3)$ and $(6,1)$.

2.2.2. Comparison on linear eigenfrequencies, mode shapes and non-linear coefficients

The linear characteristics and non-linear coupling coefficients, stemming respectively from the present model and from the shallow shell model derived in Thomas et al. (2005b), are systematically compared. The imperfection is given by Eq. (23). The variation of the eigenfrequencies is shown in Fig. 2, for increasing values of the curvature parameter χ. The modes are labeled by (k,n), where k is the number of nodal diameters and n the number of nodal circles. A perfect agreement is observed, except for the purely asymmetric modes $(k,0)$ for $k>7$. This is directly related to the truncation used in Eq. (13b). Fig. 2 has been obtained with N_w = 51 modes. They are: purely asymmetric modes from $(2,0)$ to $(10,0)$, purely axisymmetric modes from $(0,1)$ to $(0,13)$, mixed modes $(1,1)$ to $(6,1)$, $(1,2)$ to $(3,2)$ and $(1,3)$. Hence the orthoradial wave with 7 nodal diameters is represented by only one mode in the truncation, whereas two modes, $(6,0)$ and $(6,1)$, are present for the orthoradial wave with 6 nodal diameters. It has been checked that adding mode $(7,1)$ to the truncation give a perfect result for the eigenfrequency of $(7,0)$.

Profiles of two mode shapes, namely $(0,1)$ and $(2,0)$ are compared in Fig. 3, showing a very good agreement. As the imperfection introduced in the plate equation is here defined by Eq. (23), it is concluded that the higher-order terms of the Taylor expansion of the spherical imperfection have a minor effect on the linear characteristics.

Some of the non-linear cubic coefficients from the two models are now compared. Fig. 4 shows the convergence of h^u_{uuu} defined in Eq. (21) for three modes, i.e. $u=(0,1)$, $(0,2)$ and $(2,0)$, and for increasing values of χ, with respect to an increasing number of modes N_0 used to reconstruct the geometry (and for a fixed N_w equal to N_0). Whereas the cubic coefficient for mode $(2,0)$ shows a quick convergence, an important difference subsists for the two others. Moreover, for mode $(0,1)$, the converged value appears to be different from the one obtained with the shallow shell model. In order to understand the origin of this discrepancy, the cubic coefficients of modes $(0,1)$ and $(0,2)$ are compared in Fig. 5, where now the shallow shell model of Thomas et al. (2005b) is compared to the present model, where the geometric spherical imperfection is truncated to its first-order term, Eq. (25a). A very good agreement is now observed, which means that the non-linear coupling coefficients are more sensitive on the geometric imperfection than the eigenfrequencies. Inspecting back the formulas (23) and (25a), one can conclude that the present model has a larger range of application for a spherical imperfection, whereas the model developed in Thomas et al. (2005b) is more related to a parabolic shell, according to Eq. (25a). Finally, Figs. 4, 5 show that the number N_0 needed to approximate the geometry have a stronger influence on non-linear characteristics than on linear ones, as a larger N_0 is needed to obtain accuracy on the cubic coefficients. Numerous computations led on other cubic coefficients show that if $N_0=13$

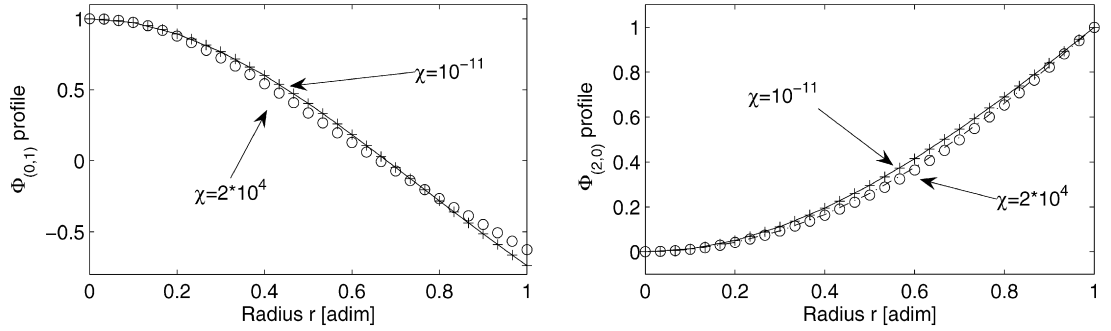

Fig. 3. Profiles of $(0,1)$ and $(2,0)$ mode shape for $\chi=10^{-11}$ and $\chi=2\times10^4$; according to the spherical shell model (Thomas et al., 2005b) ((−) and (-·-)), and to the present model ((+) and (o)).

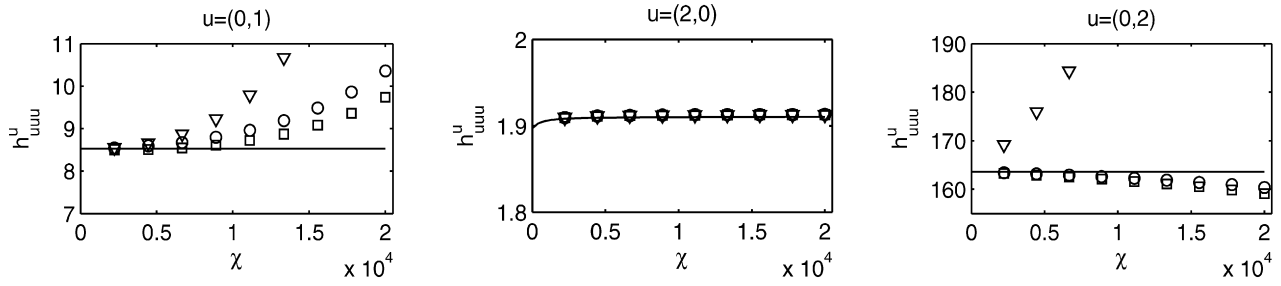

Fig. 4. Cubic coefficients h^u_{uuu} of modes $(0,1)$, $(2,0)$ and $(0,2)$ with respect to χ according to the spherical shell model (Thomas et al., 2005b) (−) and computed from the present model for $N_0=4$ (▽), $N_0=7$ (□) and $N_0=13$ (o).

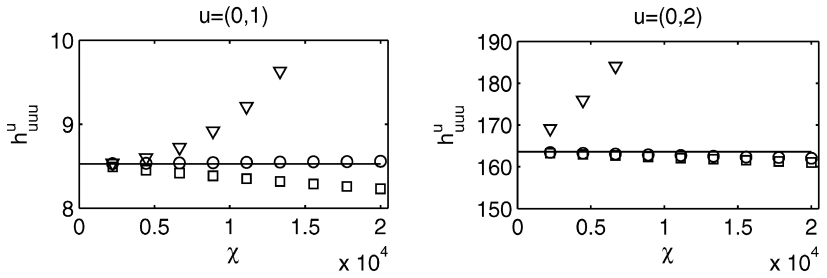

Fig. 5. Cubic coefficients h^u_{uuu} of modes $(0,1)$ and $(2,0)$ with respect to χ according to the spherical shell model (Thomas et al., 2005b) $(-)$ and computed from the present model with a spherical imperfection truncated to its leading-order term (Eq. (25a)), for $N_0 = 4$ (∇), $N_0 = 7$ $(\square)$ and $N_0 = 13$ (o).

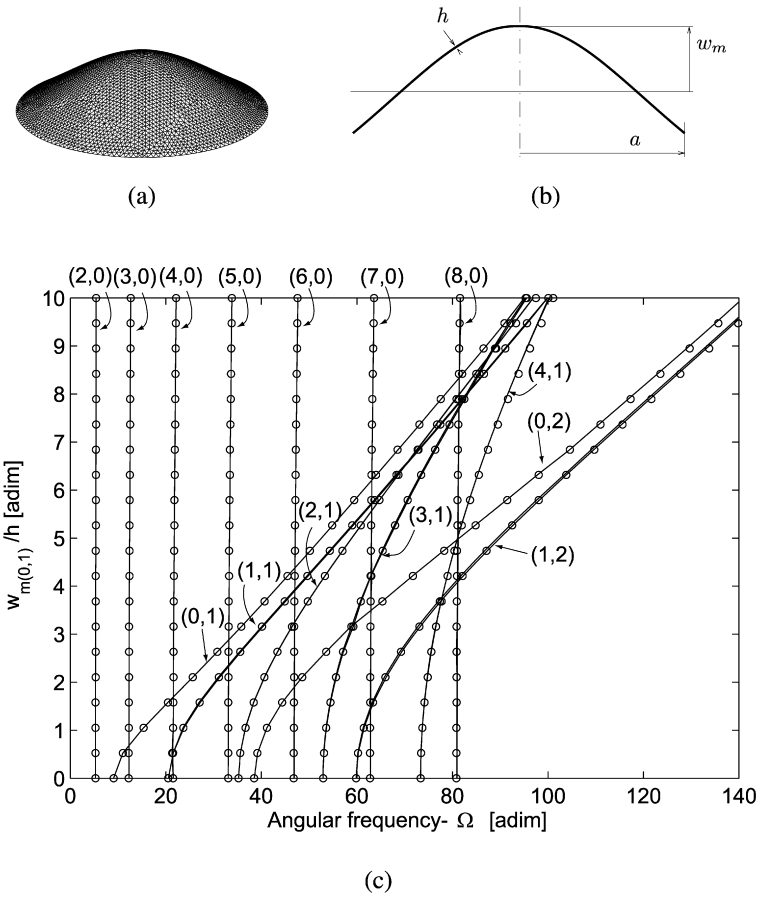

Fig. 6. (a) Finite element mesh and (b) cross-section view of the imperfection having the shape of mode $(0,1)$. (c) evolution of natural angular frequencies of the imperfect plate having the shape of mode $(0,1)$ with respect to the amplitude w_m of the imperfection normalized by h, according to CAST3M $(-)$ and calculated from the present model (o).

axisymmetric modes are kept in the truncations (i.e. from $(0,1)$ to $(0,13)$), then only a 2-digits accuracy in the non-linear coefficients is warranted, the 3-digits accuracy being reached for the majority of coefficients.

3. Results on typical imperfections

In this section, the linear characteristics predicted by the present model are compared to a numerical solution obtained with a finite elements discretization procedure, in the case of known imperfections, having successively the shape of mode $(0,1)$, $(0,2)$ and $(2,0)$, so the truncation in Eq. (13a) is reduced to $N_0 = 1$ in each case. The convergence is addressed, showing that the present model is reliable for imperfection amplitude being more than ten times the thickness with a limited number of expansion functions. The non-linear coefficients with known imperfections have been addressed in Touzé et al. (2007), where the type of non-linearity (hardening/softening behaviour) has been computed.

3.1. Imperfection having the shape of mode $(0,1)$

An axisymmetric imperfection having the shape of mode $(0,1)$ is first considered. The imperfection is shown on Fig. 6(a), (b), and writes: $w_0(r) = a_{(0,1)}\Phi_{(0,1)}(r)$, where $a_{(0,1)}$ is the only non-zero parameter in the expansion of Eq. (13a).

Fig. 6(c) shows the evolution of the first fourteen eigenfrequencies with respect to the amplitude of the imperfection w_m, defined on Fig. 6(b), from 0 (perfect plate) to ten times the thickness. The linear results provided by the present method are compared to a numerical solution obtained with the finite-element code CAST3M (Verpeaux et al., 1988) with DKT (Discrete Kirchhoff Triangle) elements (see e.g. Batoz et al. (1980) for a description of the element).

Table 1
Number N_w of axisymmetric transverse modes needed to reach the correspondent accuracy on the eigenfrequency $\Omega_{(0,1)}$ and on the diagonal cubic coefficient h^d_{ddd} of mode $d = (0, 1)$ (for an imperfection having the shape of mode $(0, 1)$, with amplitude equal to $10h$).

	3-digits accuracy	4-digits accuracy
$\Omega_{(0,1)}$ [adim]	4	6
	2-digits accuracy	3-digits accuracy
h^d_{ddd} [adim]	5	7

A 3260 finite elements mesh, shown on Fig. 6(a), has been used for the computation. A perfect agreement is found between the two solutions. One can observe that the imperfection has a huge effect on the eigenfrequencies of axisymmetric modes and mixed modes. For instance, the eigenfrequency of mode $(0, 1)$ is twice the value of the perfect plate for $w_m = 1.5h$ only. On the other hand, the eigenfrequencies of the purely asymmetric modes $(k, 0)$ are quite unchanged when increasing the imperfection.

As the problem is fully axisymmetric, the convergence of the results is investigated by increasing the number N_w of axisymmetric modes in the truncation. Table 1 shows the number N_w needed to warrant a given accuracy, for the eigenfrequency $\Omega_{(0,1)}$ as well as for the cubic non-linear coefficients h^d_{ddd}, with $d = (0, 1)$. As in the case of the spherical imperfection, it is observed that the convergence is faster for the linear characteristics. However, a good convergence is here obtained as only 7 modes are necessary to guarantee a 3-digits accuracy on the cubic coefficients. Other eigenfrequencies and other cubic coefficients have also been tested, showing the same order of magnitude for reaching convergence.

3.2. Imperfection having the shape of mode $(0, 2)$

An axisymmetric imperfection having the shape of mode $(0, 2)$ is now considered, in the same manner as in the previous section. The imperfection is shown on Fig. 7(a), (b), and writes $w_0(r) = a_{(0,2)}\Phi_{(0,2)}(r)$. Fig. 7(c) shows the evolution of the first eigenfrequencies with respect to the amplitude of the imperfection w_m, defined on Fig. 7(b). Once again, the linear results provided by the present method are compared to a numerical solution obtained with CAST3M, with the same mesh than in the previous section, shown on Fig. 7(a). A perfect agreement is found between the two solutions.

Contrary to the precedent cases (the spherical shell and the imperfection of the form of mode $(0, 1)$), the effect on the purely asymmetric modes $(k, 0)$ is not negligible now. Dimensionless eigenfrequency of $(2, 0)$, which is 5.089 for a plate reach 13.035 for an amplitude of imperfection corresponding to $10h$.

The convergence of the results is shown in Table 2 for mode $(0, 2)$. Concerning the convergence of the eigenfrequency, a limited number of modes in the expansions is sufficient to reach a fair accuracy. For the cubic coefficients, as already observed, a larger N_w is needed to attain convergence.

3.3. Imperfection having the shape of mode $(2, 0)$

The effect of an asymmetric imperfection is now investigated. For any structure with perfectly axisymmetric geometry, the eigenfrequencies associated with asymmetric modes (k, n) with $k \neq 0$ have a multiplicity of two, corresponding to two degenerated modes called *companions* or *preferential configurations* (Morand and Ohayon, 1995; Touzé et al., 2002). In the case studied here, because of the asymmetric imperfection, some eigenfrequencies of

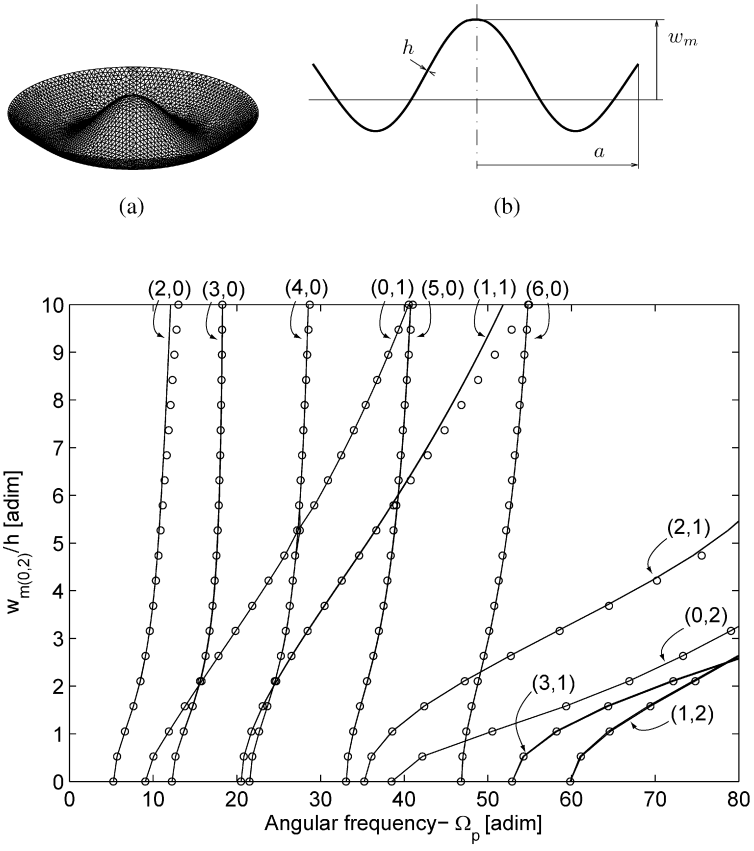

Fig. 7. (a) Finite element mesh and (b) cross-section view of the imperfection having the shape of mode $(0, 2)$. (c) Evolution of natural angular frequencies of the imperfect plate having the shape of mode $(0, 2)$ with respect to the amplitude w_m of the imperfection normalized by h, according to CAST3M $(-)$ and calculated from the present model (o).

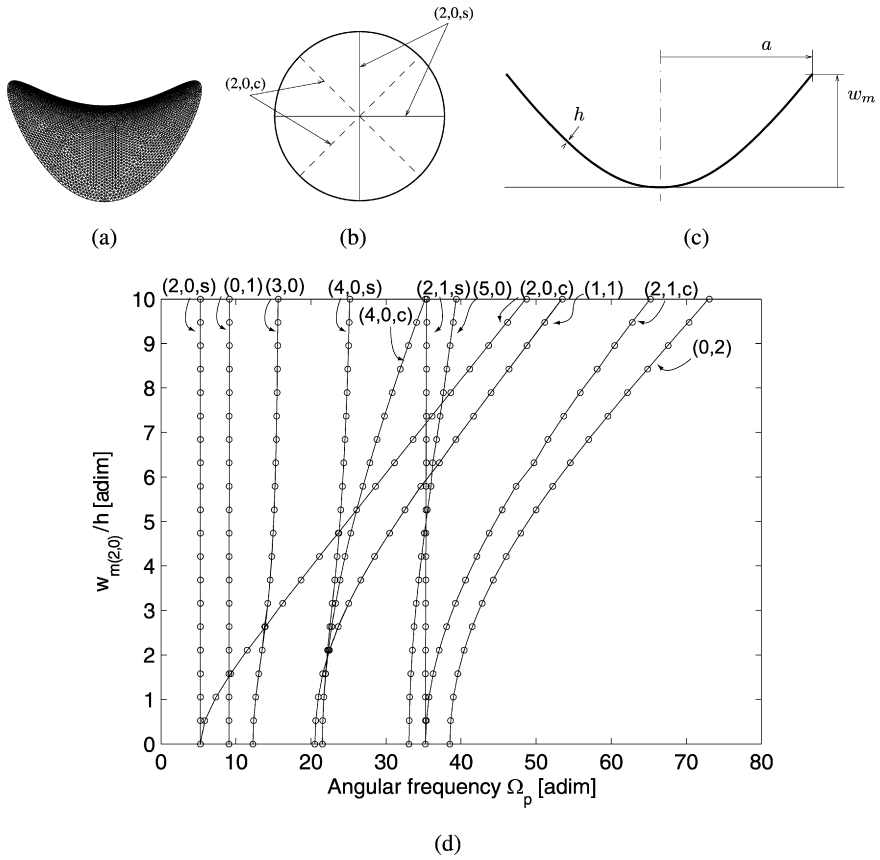

Fig. 8. (a) Finite element mesh, (b) top view with nodal radii of each configuration, (c) cross-section view of the imperfection having the shape of mode $(2,0,c)$. (d) Evolution of natural angular frequencies of the imperfect plate having the shape of mode $(2,0,c)$ with respect to the amplitude w_m of the imperfection normalized by h, according to CAST3M $(-)$ and calculated from the present model (o).

Table 2
Number N_w of axisymmetric transverse modes sufficient to reach the correspondent accuracy on the angular frequency $\Omega_{(0,2)}$ and on the diagonal cubic coefficient h^d_{ddd} of mode $d=(0,2)$ (the imperfection have the shape of mode $(0,2)$ and its amplitude is equal to $10h$).

	3-digits accuracy	4-digits accuracy
$\Omega_{(0,2)}$ [adim]	4	8
	2-digits accuracy	3-digits accuracy
h^d_{ddd} [adim]	7	8

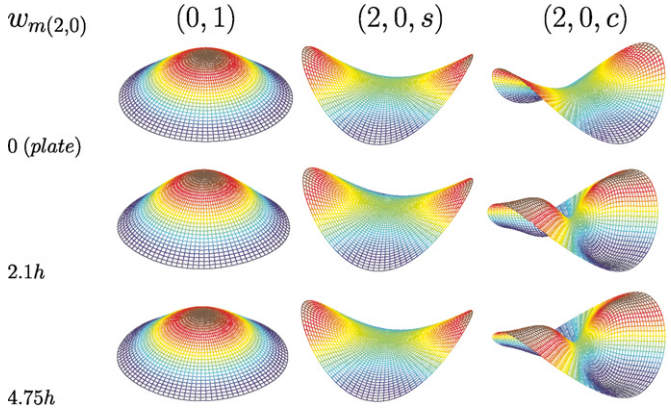

Fig. 9. Mode shapes of mode $(0,1)$, $(2,0,s)$, $(2,0,c)$ of an imperfect plate having the shape of mode $(2,0,c)$ for amplitude of imperfection $w_{m(2,0)}$ equal to 0 (perfect circular plate), $2.1h$ and $4.75h$.

degenerated modes split. Thus, distinction is systematically done between the *sine* $(\cdot,\cdot,s)$ and *cosine* $(\cdot,\cdot,c)$ configurations of companion modes. Imperfection is chosen to have the shape of mode $(2,0,c)$, and is shown in Fig. 8(a), (b). It can be written

$$w_0(r,\theta) = a_{(2,0,c)}\Phi_{(2,0,c)}(r) = a_{(2,0,c)}R_{(2,0)}(r)\cos 2\theta, \tag{28}$$

with $R_{(2,0)}(r)$ the profile of the shape, shown on Fig. 8(c).

Results on angular frequencies are reported in Fig. 8(d). A excellent agreement is observed between results from the present model and from the finite element simulation. The asymmetric imperfection have now a weighty effect on both axisymmetric and asymmetric modes. Indeed, the natural frequency of mode $(0,2)$ undergoes a huge variation, as well as the natural frequency of mode $(2,0,c)$ which is twice its value in the perfect flat plate for $w_m = 1.8h$.

Another important remark is that the influence of the imperfection is concentrated on only one of the asymmetric modes configurations, the other one keeping a constant frequency as a function of the imperfection amplitude. Moreover, only the asymmetric modes with an odd number of nodal diameters, like modes $(2,0)$, $(4,0)$, $(2,1)$ are influenced by the imperfections, which means that the symmetry is not broken for asymmetric modes having an even number of nodal diameters. Consequently, eigenfrequencies of modes $(3,0)$, $(1,1)$, $(5,0)$, ..., do not split, and their evolutions are moderate compared to the previous ones. Finally, one can note that the asymmetric mode configuration that is affected by the imperfections is always the one which degenerates from the cosine companion mode of the perfect plate.

The mode shapes for modes $(0,1)$, $(2,0,c)$ $(2,0,s)$ are shown on Fig. 9 for 3 different amplitudes of imperfection, only the mode shape of $(2,0,c)$ is largely affected. Its nodal diameters are un-

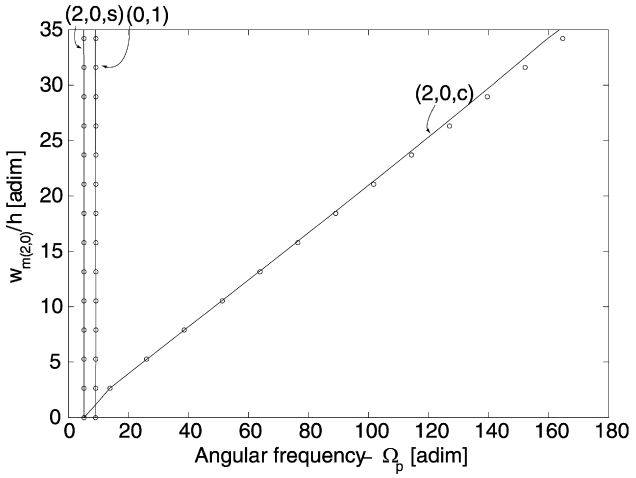

Fig. 10. Evolution of natural angular frequencies of modes $(2,0,s)$, $(0,1)$ and $(2,0,c)$, for the imperfect plate having the shape of mode $(2,0,c)$ with amplitude from 0 to $35h$, according to CAST3M (–) and computed from the present model (o).

Table 3
Number N_w of modes needed to reach the correspondent accuracy on the angular frequency Ω_d and on the diagonal cubic coefficient h^d_{ddd} of mode $d=(2,0,c)$ (the imperfection have the shape of mode $(2,0,c)$ and its amplitude is equal to $10h$).

	3-digits accuracy	4-digits accuracy
Ω_d [adim]	12	15
	2-digits accuracy	3-digits accuracy
h^d_{ddd} [adim]	25	35

changed by increasing the imperfection whereas its global shape change drastically. As their corresponding eigenfrequencies, the shape of the companion mode $(2,0,s)$, and the one of the axisymmetric mode $(0,1)$, are not influenced.

The validity of the present method is now tested for a very large amplitude of imperfection. Fig. 10 shows the evolution of natural frequencies of modes $(2,0,c)$, $(2,0,s)$ and $(0,1)$ for an imperfection amplitude up to 35 times the thickness h, compared to the finite element solution. Once again a very good agreement is observed.

As the problem is not axisymmetric anymore, asymmetric modes have to be retained in Eqs. (13b) and (17). Thus, computations are performed by keeping 51 perfect plate's transverse modes, already enumerated in Section 2.2.2. Convergence results on the angular frequency and the diagonal cubic coefficient of mode $(2,0,c)$ are reported in Table 3. Obviously, as compared to axisymmetric cases, a larger number of modes have to be retained in the truncation for guaranteeing a good accuracy. For the cubic coefficients, 25 modes are necessary for obtaining a 2-digits accuracy. It is thus observed that asymmetric imperfections are more difficult to represent, so that the present method will have some difficulties for irregular geometric imperfections, or localized defects, which would need a high number of modes to be accurately represented. This will be discussed in the next section with the application to a real shell.

4. The case of a real shell

In this section, comparisons are drawn between the prediction given by the present model and experimental measurements realized on a thin shallow spherical shell. Experimental comparisons on non-linear responses are available in the literature for some specific cases. The case of a clamped circular plates is investigated in Yamaki et al. (1981b), but axisymmetric restriction is considered, and the imperfection is of the order of one tenth the plate thickness. A good agreement is found but discrepancies are observed at large amplitudes. Raman and Mote conducted a series of experimental measurements on circular disks spinning near critical speed (Raman and Mote, 2001), but only qualitative comparisons between theory and experiments are given. For rectangular plates and circular cylindrical panels, Amabili obtained a very good agreement between experiments and theoretical predictions, with imperfection amplitudes of the order of the thickness (Amabili, 2006b, 2006a, 2008), even though by reducing the actual geometry to a single expansion function. Here we consider the real shell as an imperfect plate, so that the amplitude of the imperfection is about 28 times the thickness. Comparisons are drawn on the linear characteristics first. Then non-linear forced responses are investigated.

4.1. Measurement

A nearly spherical shell of outer diameter $2a=600$ mm and thickness $h=1$ mm, shown in Fig. 11(a)–(b), is considered. It has already been used in experiments reported in Thomas et al. (2007, 2005a), Touzé and Thomas (2005). It is made of brass, and material properties are assumed to be homogeneous and isotropic. In order to simulate free-edge boundary conditions, the shell is held with three nylon threads, fixed by means of small holes at the rim. The profile of the shell is nearly circular but curvature is not uniform and the global shape presents some asymmetric imperfections. In the above cited works, the mean curvature R_{opt} has been estimated at 1557 mm by fitting a circle to experimental points obtained with a dial comparator on a diameter of the shell. However, huge discrepancies were observed between measured eigenfrequencies and theoretical ones obtained with a spherical shell model with $R_{\text{opt}}=1557$ mm, and especially on the axisymmetric modes.

To perform a more precise analysis, the complete geometry of the shell has been measured with a coordinate measuring machine. 2842 experimental points, shown in Fig. 11(b), have been taken into account to have a fine description of the imperfection. Fig. 11(c)–(d) shows the error committed by approximating the actual shell with a spherical shell of optimal radius of curvature $R_{\text{opt}}=1557$ mm. This error is defined by:

$$e(r,\theta)=w_0(r,\theta)-w_0^{\text{th}}(r,\theta), \tag{29}$$

where $w_0(r,\theta)$ is the real (measured) geometry and $w_0^{\text{th}}(r,\theta)$ is a spherical cap of radius $R_{\text{opt}}=1557$ mm. One can observe that the error is of the order of 1.4 times the thickness of the shell.

4.2. Geometry

The measured geometry is inserted into the analysis by the following method. A Delaunay triangulation, shown in Fig. 11(b), is used to obtain a mesh of the geometry wherein the elements are built according to the experimental points of coordinates (x,y). The unknown coefficients $\{a_p\}$ of Eq. (13a) are then estimated by:

$$a_p=\iint_S \Phi_p w_0\,dS\approx\sum_i \Phi_p(x_i,y_i)z_iA_i, \tag{30}$$

where (x_i,y_i,z_i) are the coordinates of the barycenter of the i-th triangular element and A_i the area of the horizontal projection of the triangle. Fig. 12(a) shows the contribution of each function Φ_p in the expansion of this geometry. The first two axisymmetric modes $(0,1)$ and $(0,2)$ have the most proeminent participation for reconstructing the imperfection, however, as it will be shown in the remainder of the study, all the other terms with a minor participation to the reconstruction have an important influence on the forthcoming analysis. The difference between the measured geometry w_0 and the geometry w_r reconstructed with Eq. (13a) is

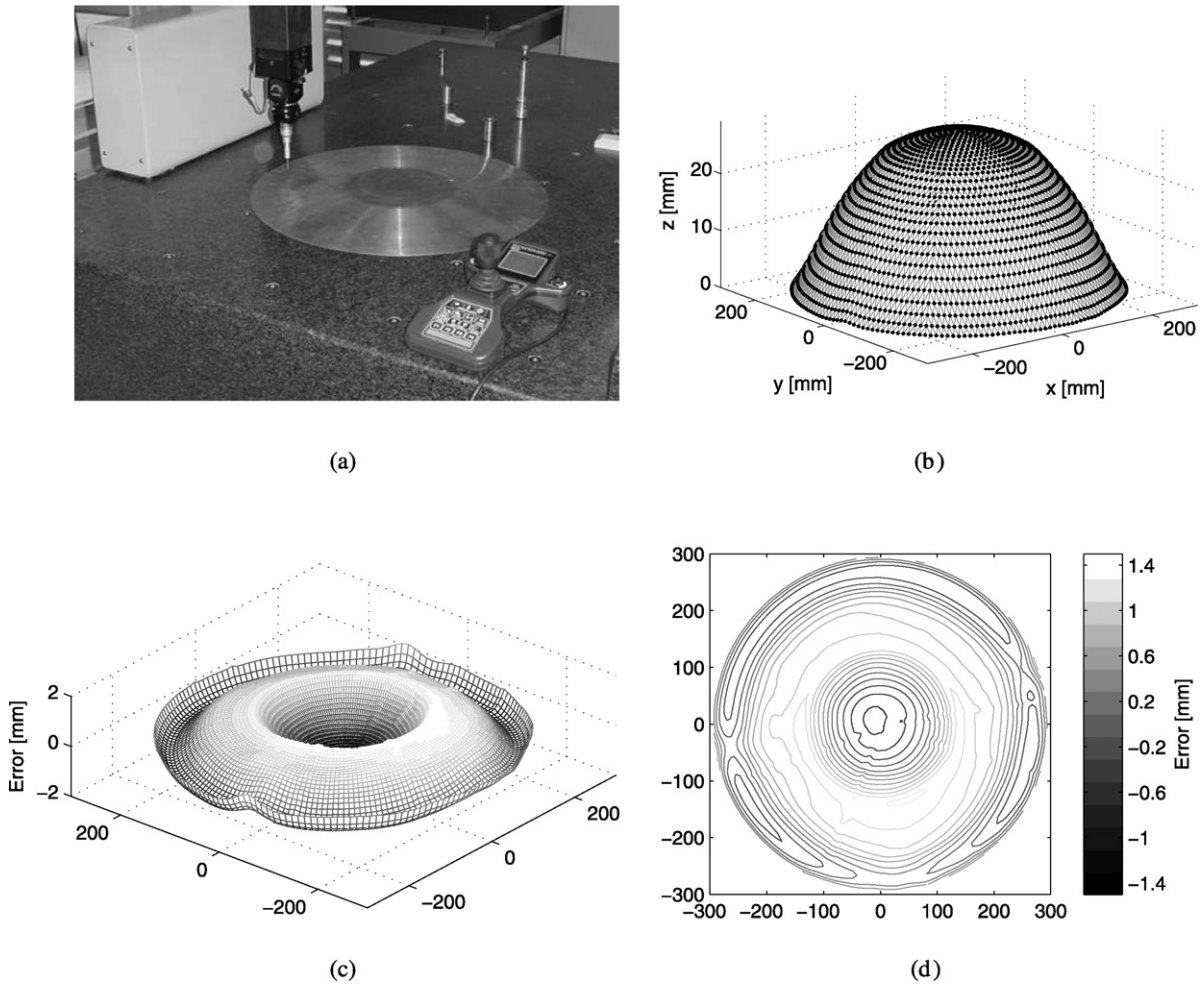

Fig. 11. Experimental set up for the measurement of the geometry of the shell. (a) Photograph of the coordinate measuring machine. (b) Three-dimensional view of the measured geometry. (c) Error in mm between the actual geometry and a spherical shell with optimal radius of curvature. (d) Contour plot of (c).

.

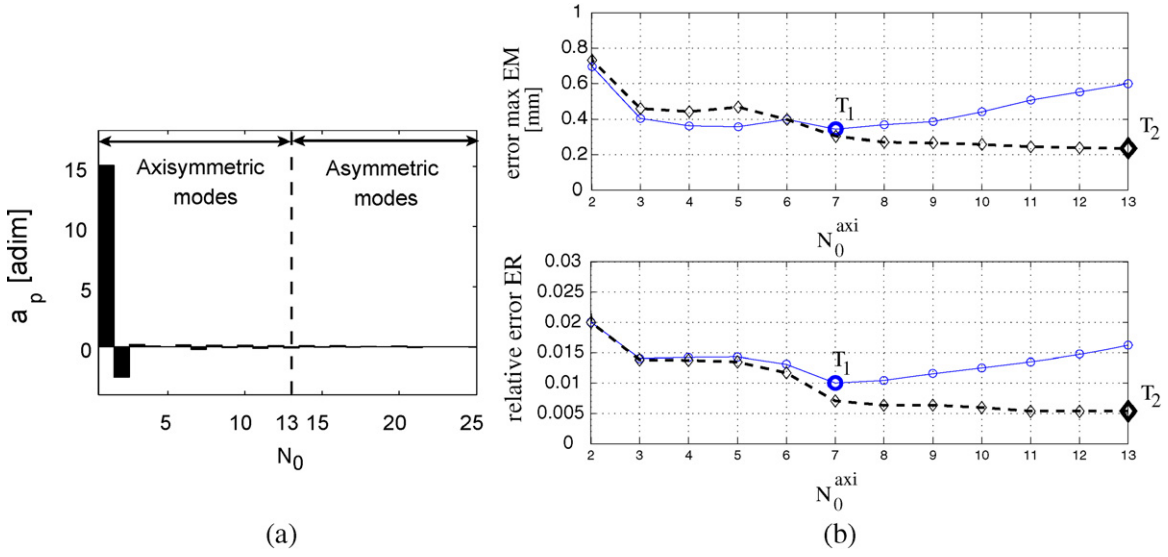

Fig. 12. (a) Expansion of the measured geometry of the shell. (b) Maximum error EM (in mm) and Relative error ER as function of the number of axisymmetric modes kept for reconstructing the geometry. Plain line: projection from the measurement points, without interpolation. Dashed line: projection with an interpolation to increase the number of computation points. $T1$ and $T2$ refers to the two truncations that are selected for further analysis.

analyzed in Fig. 12(b), where a fixed number of asymmetric modes is used in the expansion (38 asymmetric modes are used: $(2,0)$ to $(10,0)$, $(1,1)$ to $(6,1)$, $(1,2)$ to $(3,2)$ and $(1,3)$), whereas the number of axisymmetric modes N_0^{axi} is increased from 2 ($(0,1)$ and $(0,2)$) to 13 ($(0,1)$ to $(0,13)$). The maximum error *EM* and the relative error *ER* are plotted, respectively defined by:

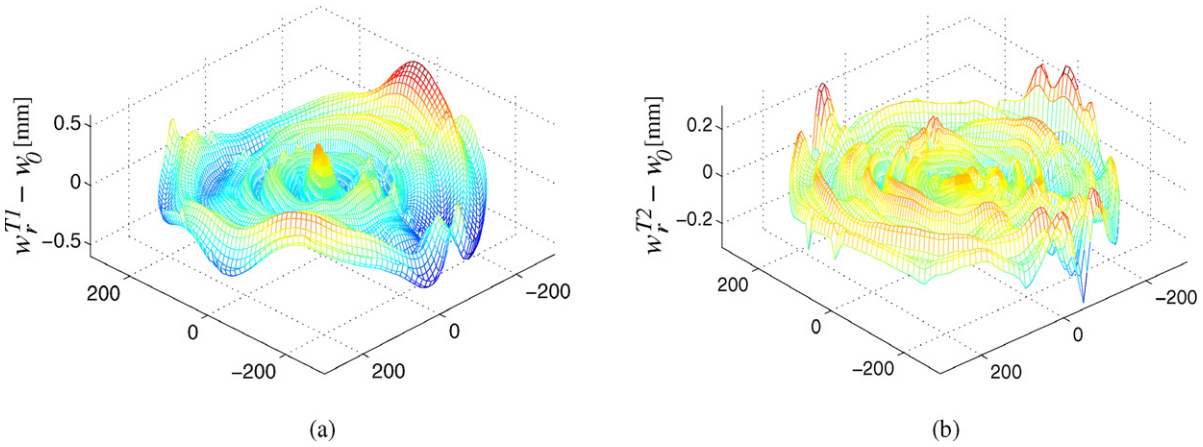

Fig. 13. Error in mm between the actual geometry and the reconstructed geometry for the two selected truncations. (a) $T1$, (b) $T2$.

$$EM = \max_{(x_i, y_i)} \left| w_0(x_i, y_i) - w_r(x_i, y_i) \right|, \tag{31a}$$

$$ER = \frac{\sqrt{\iint_S (w_0 - w_r)^2 \, dS}}{\sqrt{\iint_S w_0^2 \, dS}}. \tag{31b}$$

It is observed that the errors do not tend to zero, they first decrease but after a minimum value obtained with 7 axisymmetric modes in the expansion, the errors start to increase. This is explained by the limited number of measurement points used to compute the projection. Considering higher modes with shortened wavelength on the grid given by the 2842 measurement points leads to a loss of accuracy in the orthogonality property of the eigenvectors. This has been assessed by computing the Gram matrix composed of the inner scalar products of the functional basis, where it has been observed that out-of diagonal terms tends to have non-negligible values when considering higher modes. Hence, from mode $(0, 7)$, the orthogonality property of the basis is not well recovered and errors in the projection are made. To tackle this problem, the measured geometry has been oversampled by using a polar grid with 400 lines in the angular coordinate θ and 120 discretization points in radial coordinate r. Coefficients $\{a_p\}$ are then computed using Eq. (30), where the Delaunay triangulation is built from the oversampled mesh. The convergence, shown in dashed line in Fig. 12(b) is now better, however the maximum error has not been made less than 0.24 mm.

In the remainder of the study, two reconstructed imperfections will be analyzed. The first one, denoted by w_r^{T1} (or simply $T1$), is obtained from the computation without interpolation, and for the minimal error obtained, i.e. with all asymmetric modes and axisymmetric modes from $(0, 1)$ to $(0, 7)$. The error between w_r^{T1} and w_0 is shown in Fig. 13(a). It has mainly the shape of mode $(0, 8)$ as the logical consequence of the truncation limited to $(0, 7)$. The height at center is still badly represented with an error of 0.3 mm. Important errors are also present at the edges. The second truncation, denoted by w_r^{T2} (or simply $T2$), is obtained from the computation with interpolation, where axisymmetric modes from $(0, 1)$ to $(0, 13)$ are kept. The error is shown in Fig. 13(b). Maximum errors are still at the edge, but a limited amplitude is now observed in the center region.

4.3. Linear comparison

Eigenfrequencies and mode shapes of the present models $T1$ and $T2$ are compared against experimental measurements. A finite element modal analysis is also added to the discussion for a complete comparison. Experimental measurements have been realized by exciting the shell with an electromagnetic device composed of a magnet glued to the shell and driven by a coil. The device is fully described in Thomas et al. (2003), and the modal analysis has already been reported in Thomas et al. (2007). It is worth noting that the axisymmetric modes are measured by gluing the magnet at center of the shell. The presence of this small added mass (mass of the magnet is 6 g) lowers the axisymmetric eigenfrequencies a little bit, but this effect is limited to at most 2 Hz (Thomas et al., 2007).

Table 4
Comparison of experimental and theoretical eigenfrequencies of the shell, in Hz. Column *Experiment*: results from the experimental modal analysis. Column *Shell*: eigenfrequencies provided by the spherical shell model. Columns $T1$ and $T2$: prediction of the imperfect plate model, with truncation $T1$ and $T2$ to recover the geometry. Column CAST3M: results provided by the FE analysis.

Modes	Experiment		Shell	$T1$		$T2$		CAST3M	
$(2, 0)$	13.75	17.5	11.02	10.85	10.91	10.68	10.74	11.19	11.32
$(3, 0)$	34	35.5	26.37	25.70	25.73	25.22	25.26	26.46	26.58
$(4, 0)$	57.25	58.25	46.90	45.21	45.27	44.39	44.40	46.47	46.86
$(5, 0)$	83	83.75	72.17	68.94	69.10	67.88	67.93	71.43	71.57
$(6, 0)$	110	111	101.77	96.73	96.75	95.54	95.56	100.77	100.87
$(7, 0)$	141	141.5	135.45	132.66	132.67	132.73	132.73	134.40	134.60
$(8, 0)$	172.75	176	173.01	165.61	165.64	165.68	165.70	171.6	171.8
$(1, 1)$	259.5	271	378.4	269.20	275.07	268.27	274.31	280.89	284.65
$(0, 1)$	225		386.03	227.93		229.05		243.30	
$(0, 2)$	354		393.11	342.46		346.03		367.73	
$(0, 3)$	444.25		423.17	426.43		432.80		450.91	
$(0, 4)$	555.5		495.65	544.61		550.52		580.07	

Table 4 compares the experimental eigenfrequencies of the shell against those given by the perfect shallow shell model, the present models with truncations $T1$ and $T2$, and a finite-element model computed with CAST3M from the experimental points used to measure the geometry. The relationship between the measured natural frequencies f_p and the dimensionless theoretical angular frequencies Ω_p computed from the present model with the reconstructed geometry is:

$$f_p = \underbrace{\frac{h}{2\pi a^2}\sqrt{\frac{E}{12\rho(1-\nu^2)}}}_{f^*} \Omega_p. \tag{32}$$

Coefficient $f^* = 1.805$ Hz has been estimated by the slope of the least-square straight line of Fig. 14, obtained with truncation $T2$. Eventually, by measuring the mass of the structure, the value of the density of the material has been evaluated to $\rho = 8230$ kg m^{-3}. Using Eq. (32) with $\nu = 0.33$, one obtains $E = 97.1$ GPa for the Young's modulus of the material. The finite-element analysis has been computed by using these values for the material property. The mesh has been built with DKT elements constructed such that

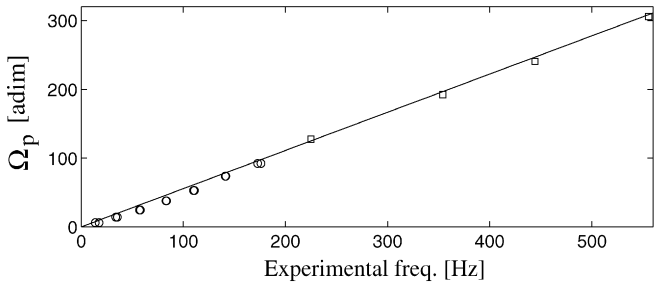

Fig. 14. Dimensionless theoretical angular frequencies Ω_p of the imperfect plate (truncation $T2$) versus the corresponding experimental natural frequencies: asymmetric modes, from $(2,0)$ to $(8,0)$ (o); axisymmetric modes, from $(0,1)$ to $(0,4)$ (□). The slope fitting line is $f^* = 1.805$ Hz.

the nodes of the mesh lie exactly at the measurement points; the computation has been realized with the software CAST3M. A second finite-element analysis, not reported here, have also been conducted with the software MSC-NASTRAN with the same procedure, providing coincident results as the ones given by CAST3M.

The results summarized in Table 4 show the improvement brought by the present model, as compared to the predictions given by the perfect spherical shell model (Thomas et al., 2005b) with $R_{opt} = 1557$ mm. Whereas the perfect shell model gives incorrect values for axisymmetric modes, taking into account more precisely the geometry allows to recover these eigenfrequencies. On the other hand, the finite-element model overpredict axisymmetric eigenfrequencies. One can also remark that the results provided by truncations $T1$ and $T2$ are very close, so that the gain in the approximation of the geometry between these two models has only a slight influence on the linear characteristics. Finally, some discrepancies subsist between the different models and the measurements. The splitting of the two companion configurations for $(2,0)$, that are separated by 3.75 Hz in the measurement, is not reproducted by any model, all of them predicting close eigenfrequencies for the two configurations of $(2,0)$. On the other hand, the splitting for mode $(1,1)$ is better predicted by the models, though still underestimated. The spacing between the asymmetric eigenfrequencies is also not correctly respected, all of them appearing lower in the theory than in the measurements. All these results may be explained by the error in the approximation of the geometry. However, considering the slight improvement obtained between truncations $T1$ and $T2$, the most probable cause of the discrepancy could be another imperfection that has not been taken into account in the model, such as a material inhomogeneity or a variation of the thickness. This will be further discussed in the next subsection with the non-linear results.

In addition to the best approximation of the eigenfrequencies, the mode shapes are also better recovered with the present model. Fig. 15 shows the measured deflection shape for modes $(3,0)$, $(0,1)$, $(0,2)$ and $(1,1)$. They are compared against the mode shapes predicted by the perfect spherical shell model and by the present model with truncation $T2$. The results given by truncation $T1$ and by the FE analysis for the mode shapes are very similar so that only one is shown. For the purely asymmetric mode $(3,0)$, measurement is coincident with the shallow shell model as well as with the present model. The same matching has been found for the other purely asymmetric modes $(k,0)$, with $k = 2$ to 9. On the other hand, for modes $(0,1)$, $(0,2)$ and $(1,1)$, the present model allows recovering finely the measured deflection shapes.

4.4. Non-linear comparison

4.4.1. The 1:1:2 internal resonance

The present model of the imperfect plate is now used to fit experimental frequency-response curves in the non-linear range,

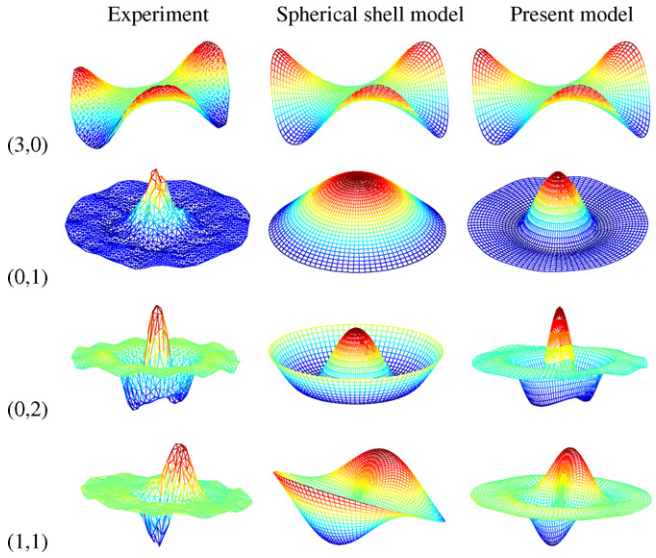

Fig. 15. Comparison of experimental deflection shapes (first column), mode shapes predicted by the perfect spherical shell model (second column) and by the present model (third column), for modes $(3,0)$, $(0,1)$, $(0,2)$ and $(1,1)$.

with the structure subjected to harmonic excitation. A peculiarity of the present shell is that it displays a 1:1:2 internal resonance: the eigenfrequency of mode $(0,1)$ is approximately twice the value of the two companion asymmetric eigenfrequencies of mode $(6,0)$. This 1:1:2 resonance has been thoroughly studied, on the theoretical viewpoint in Thomas et al. (2005b), as well as on the experimental viewpoint (Thomas et al., 2007), where a full measurement campaign had been done for various cases. The experimental data obtained in Thomas et al. (2007) will be used here to compare with the predictions of the present model. Experimental procedures and the main features of the 1:1:2 internal resonance are first briefly recalled.

Truncating the equations of motion to the three modes involved in the 1:1:2 resonance, and keeping the resonant non-linear quadratic coefficients only, gives the simplest reduced-order model that is able to reproduce the fine and complex phenomenology of the resonance curves, see Thomas et al. (2007). The reduced order model reads:

$$\begin{aligned}
&\ddot{q_1} + \omega_1^2 q_1 = \varepsilon[\alpha_1 q_1 q_3 - 2\mu_1 \dot{q_1}],\\
&\ddot{q_2} + \omega_2^2 q_2 = \varepsilon[\alpha_2 q_2 q_3 - 2\mu_2 \dot{q_2}],\\
&\ddot{q_3} + \omega_3^2 q_3 = \varepsilon\left[\alpha_3 q_1^2 + \alpha_4 q_2^2 - 2\mu_3 \dot{q_3} + Q\cos(\omega t)\right],
\end{aligned} \tag{33}$$

with

$$\begin{aligned}
&\alpha_1 = -g_{13}^1 - g_{31}^1 = \alpha_2 = -g_{23}^2 - g_{32}^2 \quad \text{and}\\
&\alpha_3 = -g_{11}^3 = \alpha_4 = -g_{22}^3.
\end{aligned} \tag{34}$$

where the subscripts 1, 2 and 3 refers respectively to mode $(6,0,c)$, $(6,0,s)$ and $(0,1)$. The shell is excited at center so that the forcing term appears only on the third equation. Q is the forcing amplitude, and ω the driving frequency, which is in the vicinity of ω_3. A detailed analysis of Eqs. (33) is provided in Thomas et al. (2005b) with a multiple scales analysis. Analytical expression for all the solution branches are found. It shows, amongst other things, that energy transfers are possible from mode $(0,1)$ to $(6,0,c)$ (i.e. $q_1 \neq 0$ and $q_3 \neq 0$, $q_2 = 0$, denoted by C1 coupling), or to $(6,0,s)$ (i.e. $q_2 \neq 0$ and $q_3 \neq 0$, $q_1 = 0$, denoted by C2 coupling), but not simultaneously. Instability regions are found to depend only on $\{\omega_1, \mu_1, \alpha_1\}$ for C1 coupling, and on $\{\omega_2, \mu_2, \alpha_2\}$ for C2 coupling. By fitting experimental instability regions and solutions branches

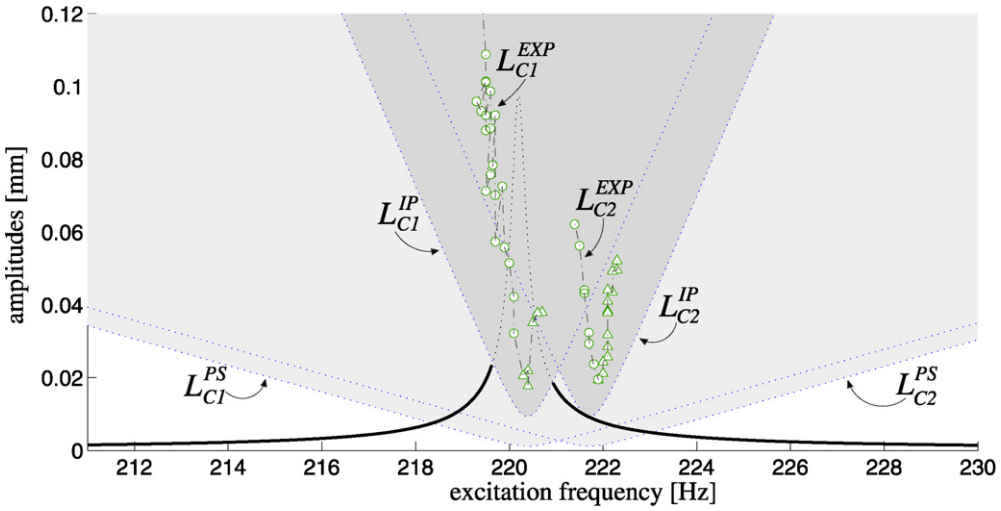

Fig. 16. Frequency-response curve and instability regions of the shell, harmonically forced in the vicinity of mode (0,1). Sdof solution in solid black. Grey-shaded are instability regions, for the perfect spherical shell model (light grey), and for the imperfect plate model (deep grey). Lowerscripts $C1$ and $C2$ refer to the coupling encountered, whereas upperscripts denote respectively: PS for Perfect Shell model, IP for Imperfect Plate (present) model, EXP for experimental measurements, obtained by increasing sweep (∘) and decreasing sweep (△) in Thomas et al. (2007).

to measurements, all the coefficients of the reduced model given by Eqs. (33) have been estimated in Thomas et al. (2007). In particular, it was found that the quadratic coefficients $\{\alpha_i\}_{i=1,4}$ were 30 times smaller than the values predicted by the perfect spherical shell model.

4.4.2. Influence of quadratic coefficients

Table 5 summarizes the values obtained for the quadratic coefficients $\{\alpha_i\}_{i=1,4}$, computed with Eqs. (34), (22a), (19a), (19b) and the measured geometry reconstructed with truncations $T1$ and $T2$. One can remark the large improvement provided by the present model as compared to the perfect spherical shell model. The two coefficients α_3 and α_4 are now finely predicted. However, the error committed on coefficients α_1 and α_2, though reduced from a factor 30 to a factor 5, is still present.

This error is further analyzed in Fig. 16, where the instability regions are reported on the frequency-response curve, for the two theoretical models, i.e. the perfect shell model and the present imperfect plate model with truncation $T2$. The single degree-of-freedom solution (sdof branche for $q_1 = q_2 = 0$, $q_3 \neq 0$) is linear since the reduced model (33) without cubic term is used. The eigenfrequencies ω_1, ω_2 and ω_3 have been fixed to their measured values to obtain a good tuning of the 1:1:2 internal resonance. Since the damping values have the same order of magnitudes for the modes, the shape of the instability regions is completely controlled by the values of α_1 and α_2. Fig. 16 shows the important improvement brought by considering the present model: for this level of forcing (0.138 N), the perfect shell model predicts C1 and C2 coupling, whereas only C1 coupling is present, as recovered by the present model. However the factor five error still present in coefficients α_1 and α_2 prevent recovering the experimental results perfectly, so that the predicted instability regions, though better, are still not exactly coincident with the measurement.

Table 5
Experimental and theoretical values of the quadratic coupling coefficients $\{\alpha_i\}_{i=1,4}$ defined by Eqs. (33), where non-dimensional equations are obtained by dividing the transverse displacement by the thickness, so that $\varepsilon = 12(1-\nu^2)$ for the present model, truncation $T1$ and $T2$ (from Eq. (12)), whereas $\varepsilon = 12(1-\nu^2)\frac{a^2}{Rh}$ for the perfect shell model and the experimental values (Thomas et al., 2005b, 2007).

	Experience	Spherical shell	$T1$	$T2$
$\varepsilon\alpha_1$	476	19057	2556	2297
$\varepsilon\alpha_2$	455	19057	2552	2294
$\varepsilon\alpha_3$	635	8766	666	608
$\varepsilon\alpha_4$	667	8766	665	607

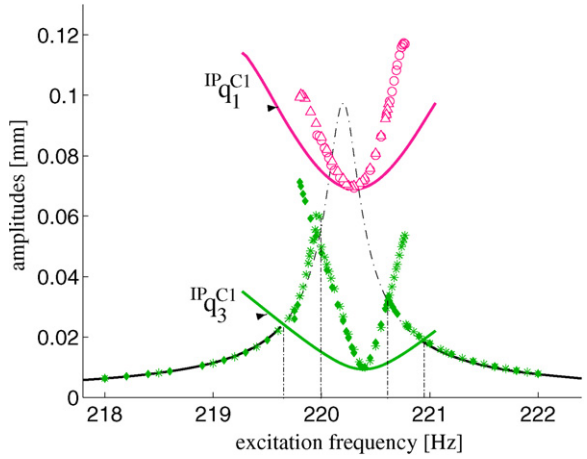

Fig. 17. Frequency-response curve of the shell, harmonically forced in the vicinity of mode (0, 1), amplitude of excitation 0.138 N. Measurements obtained by increasing sweep ((o) for $q1$, (∗) for $q3$) and decreasing sweep ((△) for $q1$ and (◇) for $q3$) are compared to the solution branches (respectively $^{IP}q1^{C1}$ and $^{IP}q3^{C1}$) obtained by the present (Imperfect Plate) model.

Solution branches for this level of forcing (0.138 N) are reported in Fig. 17. The damping values have been adjusted to obtain a correct fit on the length of the branches. The error committed on coefficient α_1 gives here a more wide-mouthed coupled branch for $^{IP}q_3^{C1}$ (the right upperscript refers to the coupling $C1$ encountered, the left upperscript IP to the model used, i.e. the imperfect plate mode). However the coupled branch for $^{IP}q_1^{C1}$ is near measurements.

The convergence of two quadratic coefficients, α_1 and α_3, with respect to N_w^{axi} is shown in Fig. 18, where N_w^{axi} is defined in the same manner as in Fig. 12(b): the first 38 asymmetric modes of the perfect plate are retained, and the number of axisymmetric modes is increased from 1 (mode $(0,1)$) to 13 (mode $(0,1)$ to $(0,13)$). This figure shows a quick convergence of the coefficients with respect to the axisymmetric expansion. A similar study shows that the convergence versus the asymmetric terms of the expansion was also of good quality, so that the truncation with respect

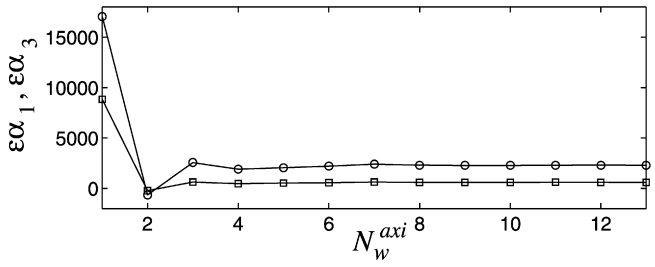

Fig. 18. Convergence of the numerical values of quadratic resonant terms $\varepsilon\alpha_1$ (○) and $\varepsilon\alpha_3$ (□) of Table 5, versus N_w^{axi}, the number of axisymmetric terms retained in Eq. (13b).

to N_w is not involved for explaining the discrepancy observed on quadratic coefficients α_1 and α_2.

4.4.3. Influence of cubic coefficients

Finally, the cubic coefficients are retained in the dynamical equations to simulate more precisely the imperfect plate behaviour as well as to evaluate their influence on the non-linear shell response. As the quadratic terms will not change, the discrepancy in the instability region is still present. The frequency-response curve is shown in Fig. 19, for a lower value of the forcing amplitude (0.0277 N). The complete model including cubic terms is described by Eqs. (21). The solution branches are computed numerically using the software AUTO Doedel et al. (2002). They are denoted on Fig. 19 with the left upperscript IC (for Imperfect plate model with Cubic coefficients). The solution branches given by the reduced equations (33) are denoted with the left upperscript IQ (Imperfect with Quadratic coefficients only). The convergence of the numerical solution has been carefully studied by raising the number of terms N_w in the AUTO-simulations. The results presented have been obtained for $N_w = 13$, where the selected modes are: $(2,0)$ to $(6,0)$, $(0,1)$ to $(0,3)$. The results with 13 modes were quite coincident to those obtained with only the 3 modes involved in the internal resonance, for vibration amplitude up to h. A very fine model composed of 22 modes (not shown) has also been tested in order to have full confidence in the converged values given by the 13-dofs model, no visible discrepancies have been observed.

For this level of forcing amplitude, 0.0277 N, the model predicts C1 coupling, whereas the experiments do not show any coupling. This is related to the overprediction of α_1. However, as compared to the results given by the model truncated to quadratic terms, the model with cubic non-linear terms shows important qualitative improvements that were all found in the experiments. First, as shown on Fig. 19, the model with cubic terms shows a slight softening behaviour. This softening type non-linearity is slightly visible on the experimental points, that are on the left of the linear sdof ${}^{\text{IQ}}q_3{}^{\text{sdof}}$ solution. The softening-type non-linearity has been more clearly assessed experimentally by adding a small mass at center of the shell, hence lowering the eigenfrequency ω_3 of mode $(0,1)$. By doing so, mode $(0,1)$ is moved away from 1:1:2 resonance and its sdof behaviour has been measured, showing a clear softening-type behaviour, see Thomas et al. (2007). Hence the full model predicts the correct type of non-linearity, however as shown on Fig. 19 the softening behaviour is overestimated.

The second important fact displayed by the complete model with cubic non-linear terms is that the branch of coupled solutions for q_3 is not anymore coincident with the boundary of the C1 instability region, as it was the case for the model truncated to quadratic terms solved by the multiple scales method. This qualitative behaviour has been clearly observed in the experiments, but for higher vibratory levels than the ones simulated here, see Thomas et al. (2007).

Finally, cubic terms influence the shape of the solution branches by increasing the curvature at their upper and lower frequency limits. It can be observed on Fig. 19 by comparing ${}^{\text{IQ}}q_1{}^{C1}$ and ${}^{\text{IC}}q_1{}^{C1}$ around 220.6 Hz. Again, this qualitative behaviour has been clearly observed in the experiments and was a cause of mismatch between the experiments and the theoretical model of Thomas et al. (2007).

Hence this complete model shows a good qualitative behaviour as compared to experiments, but it appears that some of the cubic coefficients may be overestimated also, so that the typical non-linear effect are given for too small vibration amplitudes as compared to the experiments.

4.5. Discussion

To conclude on this experimental comparisons, although the results are significantly improved as compared to the perfect shell model, some discrepancies still subsist. The eigenfrequencies are well estimated, but a perfect prediction has not been made possible. At the non-linear level, some quadratic coefficients are overpredicted so that instability regions are not perfectly fitted to experimental ones. The cubic coefficients show an improvement in the qualitative behaviour, however some of them are also to be

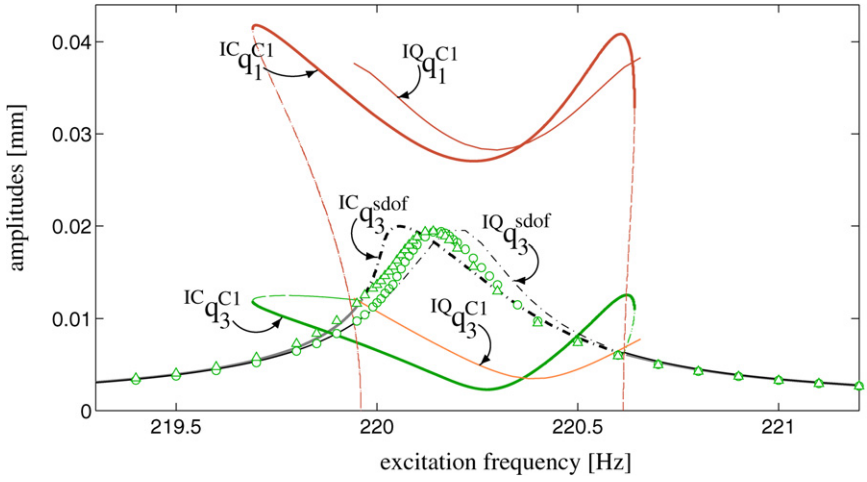

Fig. 19. Frequency-response curve of the shell, harmonically forced in the vicinity of mode (0,1), amplitude of excitation 0.0277 N. The results given by the imperfect plate model with cubic term (left upperscript IC) are compared to those given by the same model with quadratic terms only (left upperscript IQ) and to the experimental points (o: increasing frequency sweep, △: decreasing frequency sweep).

overpredicted, so that the non-linear behaviour appears for forcing levels that are below the ones encountered in the experiment.

The first reason should be the approximation of the geometry. It has been shown in Section 4.2 that despite an enrichment of the measured geometry with interpolation points, a small error at the projection step were still present, though severely reduced. Secondly, these investigations have shown that when converging to the minimum error, the convergence rate of the linear and non-linear results were slower and slower. Consequently, another improvement of the approximation of the geometry should have a limited effect on the results presented here. Another option could be that a too large imperfection amplitude had been added to the model. However, by comparison with numerical results of Sections 2 and 3, one can see that the present shell is not specifically out of range as compared to the imperfection amplitudes theoretically tested. The aspect ratio χ (defined by Eq. (27)) of the actual shell, with $R_{\text{opt}} = 1.557$ mm, is $\chi = 3.6 \cdot 10^4$, which is in the range covered by Fig. 2. Secondly, the results given by the finite element codes with shell elements have not been found better than the ones obtained with our model, hence discarding this possibility. Finally, the most probable reason for the observed discrepancy is the presence of a non-modelled imperfection in the actual shell, that has important consequences, especially for the non-linear coefficients. A variation of the thickness of the shell could be involved, or an inhomogeneity in material properties due to manufacturing process.

5. Conclusion

Effect of geometric imperfections on linear and non-linear characteristics of thin circular plates with free-edge have been studied. Thanks to Galerkin expansion by using the eigenmodes of the perfect plates, equations of motion of the imperfect plates are written in a concise form which allows an easy and effective computation. The main advantage of the present method is that linear as well as non-linear coefficients are found directly from the cubic non-linear coefficients of the perfect plate only. The method developed in this paper oversteps the modeling limitations often found in previously published works, such as the axisymmetric restriction or the expansion to only one mode in the Galerkin procedure. Moreover, convergence questions have been systematically addressed. It has been found that for axisymmetric imperfections, a quick convergence is obtained so that a limited number of expansion functions are needed to compute linear and non-linear characteristics. However, for asymmetric imperfections, the number of expansion functions rapidly increases, so that the method may have some difficulties to accurately represent asymmetric imperfect plates with non-regular or localized imperfections. Finally, numerical results show that the present method can be used to model a shallow shell as a plate with a large imperfection amplitudes, more than ten times the thickness.

Comparison with a real shell shows a good agreement on linear characteristics. At the non-linear level, an important improvement is obtained as compared to a perfect spherical shell model. However some discrepancies subsist. A careful study if this mismatch shows that its effect is more pronounced on non-linear terms, which is in the line of the theoretical results presented, where convergence is shown to be more difficult for non-linear characteristics than for linear ones. A global overprediction of non-linear coefficients seems to be at hand, resulting in overprediction of the instability region and the type of non-linearity, though given of the correct, softening type. A detailed analysis of the discrepancy has been made, showing that the error committed on the reconstructed geometry could be a factor, but the most probable option is that another imperfection such as a variation of the thickness or an inhomogeneous material property is present in the tested shell.

Acknowledgements

The authors would like to thank Pierre Breteau, François Thiebaut and Olivier De Smet for the rapid and very precise measurements of the whole geometry of circular plates and spherical shells performed in LURPA, Cachan, France. Gilles Fay is thanked for discussions on orthogonality and discretization, and Lionel Auffray for his efficient and quick help in finite-element modal analysis.

References

Amabili, M., 2003. Theory and experiments for large-amplitude vibrations of empty and fluid-filled circular cylindrical shell with imperfections. Journal of Sound and Vibration 262 (4), 921–975.

Amabili, M., 2006a. Theory and experiments for large-amplitude vibrations of circular cylindrical panel with geometric imperfections. Journal of Sound and Vibration 298 (1-2), 43–72.

Amabili, M., 2006b. Theory and experiments for large-amplitude vibrations of rectangular plates with geometric imperfections. Journal of Sound and Vibration 291 (3-5), 539–565.

Amabili, M., 2008. Nonlinear Vibrations and Stability of Shells and Plates. Cambridge University Press.

Amabili, M., Païdoussis, M.P., 2003. Review of studies on geometrically nonlinear vibrations and dynamics of circular cylindrical shells and panels, with and without fluid-structure interaction. ASME Applied Mechanical Review 56 (4), 349–381.

Batoz, J.-L., Bathe, K.-J., Ho, L.-W., 1980. A study of three-node triangular plate bending elements. International Journal for Numerical Methods in Engineering 15 (12), 1771–1812.

Celep, Z., 1976. Free flexural vibration of initially imperfect thin plates with large elastic amplitudes. ZAMM 56, 423–428.

Chen, C.S., Cheng, W.S., Tan, A.H., 2005. Non-linear vibration of initially stressed plates with initial imperfections. Thin-Walled Structures 43, 33–45.

Chia, C.Y., 1980. Nonlinear Analysis of Plates. McGraw-Hill, New-York.

Coppa, A.P., 1966. Measurement of initial geometrical imperfection of cylindrical shells. AIAA Journal 4 (1), 172–175.

Doedel, E., Paffenroth, R., Champneys, A., Fairgrieve, T., Kuznetsov, Y., Oldeman, B., Sandstede, B., Wang, X., 2002. Auto 2000: Continuation and bifurcation software for ordinary differential equations. Tech. rep., Concordia University.

Donnell, L.H., 1976. Beams, Plates and Shells. McGraw-Hill, New-York.

Gonçalves, P.B., 1994. Axisymmetric vibrations of imperfect shallow spherical caps under pressure loading. Journal of Sound and Vibration 174 (2), 249–260.

Gupta, U.S., Lal, R., Sharma, S., 2007. Vibration of non-homogeneous circular Midlin plates with variable thickness. Journal of Sound and Vibration 302, 1–17.

Hui, D., 1983. Large-amplitude axisymmetric vibrations of geometrically imperfect circular plates. Journal of Sound and Vibration 2 (91), 239–246.

Hui, D., 1984. Effects of geometric imperfections on large-amplitude vibrations of rectangular plates with hysteresis damping. ASME Journal of Applied Mechanics 51, 216–220.

Hui, D., Leissa, A.W., 1983. Effects of geometric imperfections on vibrations of biaxially compressed rectangular flat plates. ASME Journal of Applied Mechanics 50, 750–756.

Ilanko, S., 2002. Vibration and post-buckling of in-plane loaded rectangular plates using a multiterm Galerkin's method. ASME Journal of Applied Mechanics 69, 589–592.

Koiter, W.T., 1963. The effect of axisymmetric imperfections on the buckling of cylindrical shell under axial compression. Proceedings of the Koninklijke Nederlandse Akademie van Wetenschappen, serie B 66, 265–279.

Kubenko, V.D., Koval'chuk, P.S., 2004. Influence of initial geometric imperfections on the vibrations and dynamic stability of elastic shells. International Applied Mechanics 40, 847–877.

Lin, C.C., Chen, L.W., 1989. Large-amplitude vibration of an initially imperfect moderately thick plate. Journal of Sound and Vibration 135 (2), 213–224.

Morand, H.J.-P., Ohayon, R., 1995. Fluid Structure Interaction. Wiley.

Nayfeh, A.H., Nayfeh, J.F., Mook, D.T., 1992. On methods for continuous systems with quadratic and cubic nonlinearities. Non-linear Dynamics 3, 145–162.

Ostiguy, G.L., Sassi, S., 1992. Effects of initial geometric imperfections on dynamic behaviour of rectangular plates. Non-linear Dynamics 3, 165–181.

Raman, A., Mote Jr., C.D., 2001. Experimental studies on the non-linear oscillations of imperfect circular disks spinning near critical speed. International Journal of Non-linear Mechanics 36 (2), 291–305.

Rosen, A., Singer, J., 1974. Effect of axisymmetric imperfections on the vibrations of cylindrical shells under axial compression. AIAA Journal 12, 995–997.

Rosen, A., Singer, J., 1976. Effect of asymmetric imperfections on the vibrations of axially compressed cylindrical shells. Israel Journal of Technology 14, 23–36.

Thomas, O., Touzé, C., Chaigne, A., 2003. Asymmetric non-linear forced vibrations of free-edge circular plates, part II: experiments. Journal of Sound and Vibration 265 (5), 1075–1101.

Thomas, O., Luminais, E., Touzé, C., 2005a. Non-linear modal interactions in free-edge thin spherical shells: measurements of a 1:1:2 internal resonance. In: Proceedings of the Third MIT Conference on Computational Fluid and Solid Mechanics. Boston.

Thomas, O., Touzé, C., Chaigne, A., 2005b. Non-linear vibrations of free-edge thin spherical shells: modal interaction rules and 1:1:2 internal resonance. International Journal of Solids and Structures 42 (11–12), 3339–3373.

Thomas, O., Touzé, C., Luminais, E., 2007. Non-linear vibrations of free-edge thin spherical shells: experiments on a 1:1:2 internal resonance. Non-linear Dynamics 49 (1–2), 259–284.

Tobias, S.A., 1951. A theory of imperfection for the vibration of elastic bodies of revolution. Engineering 172, 1409–1420.

Touzé, C., Thomas, O., August 2005. Type of non-linearity of shallow spherical shells using non-linear normal modes. In: Proc. of Fifth Euromech Non-linear Dynamics Conference, ENOC 2005. Eindhoven, pp. 852–861.

Touzé, C., Thomas, O., Chaigne, A., 2002. Asymmetric non-linear forced vibrations of free-edge circular plates, part I: theory. Journal of Sound and Vibration 258 (4), 649–676.

Touzé, C., Thomas, O., Chaigne, A., 2004. Hardening/softening behaviour in non-linear oscillations of structural systems using non-linear normal modes. Journal of Sound and Vibration 273 (1–2), 77–101.

Touzé, C., Camier, C., Favraud, G., Thomas, O., 2007. Effect of imperfections and damping on the type of non-linearity of circular plates and shallow spherical shells. Mathematical Problems in Engineering, vol. 2008, Article ID 678307, 19 pages, doi:10.1155/2008/678307, 2008.

Verpeaux, P., Charras, T., Millard, A., 1988. Calcul des structures et intelligence artificielle. Pluralis, (Ed.), Paris, http://www-cast3m.cea.fr, Ch. CASTEM 2000: Une approche moderne du calcul des structures (in French).

Yamaki, N., Chiba, M., 1983. Non-linear vibrations of a clamped rectangular plate with initial deflection and initial edge displacement, part I: Theory. Thin-Walled Structures 1 (1), 3–29.

Yamaki, N., Otomo, K., Chiba, M., 1981a. Non-linear vibrations of a clamped circular plate with initial deflection and initial edge displacement, part I: Theory. Journal of Sound and Vibration 79, 23–42.

Yamaki, N., Otomo, K., Chiba, M., 1981b. Non-linear vibrations of a clamped circular plate with initial deflection and initial edge displacement, part II: Experiment. Journal of Sound and Vibration 79, 43–59.

Yamaki, N., Otomo, K., Chiba, M., 1983. Non-linear vibrations of a clamped rectangular plate with initial deflection and initial edge displacement, part II: Experiment. Thin-Walled Structures 1 (1), 101–119.